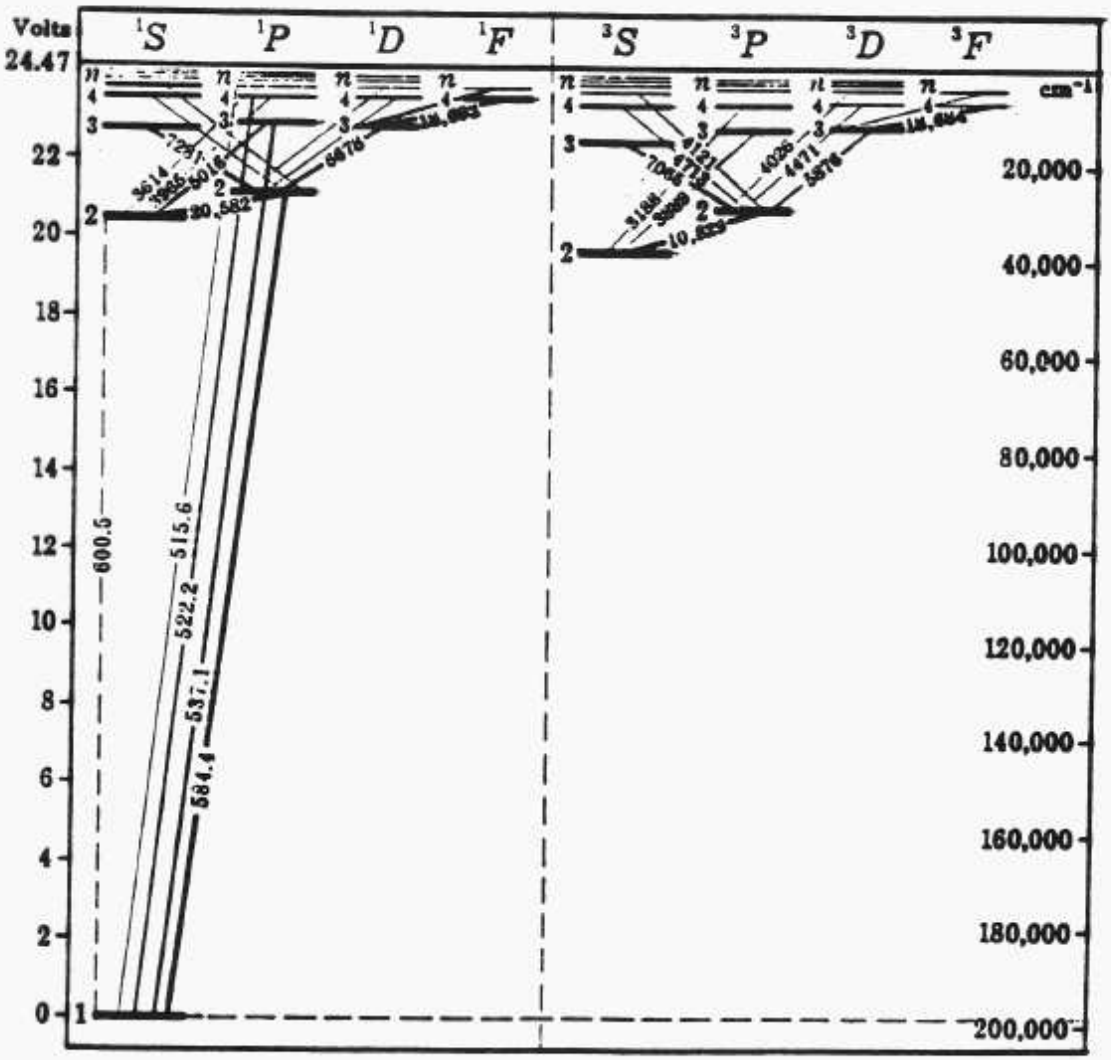

Fig. 27. Energy Level Diagram for Helium. The running numbers and true principal quantum numbers of the emission electron are here identical. The series in the visible and near ultraviolet regions correspond to the indicated transitions between terms with $n \geqq 2$.

[23] The weak intercombination line reported by Lyman at 591.6 Å is an Ne line according to Dorgelo (55).

Fig. 1.—

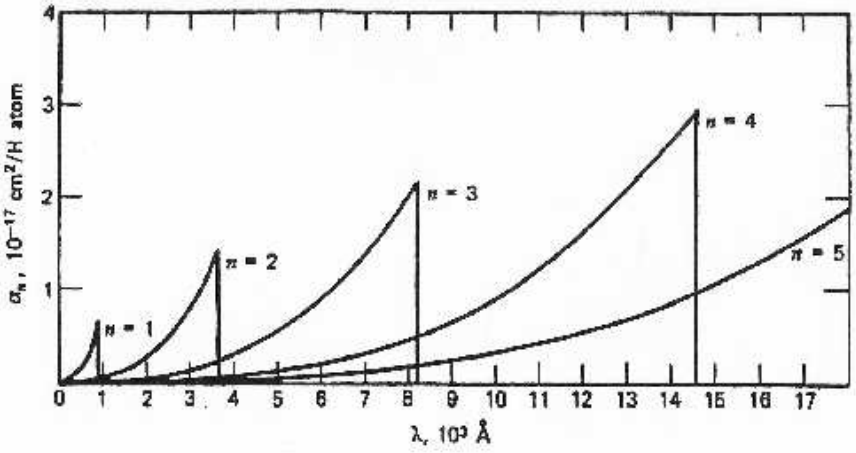

Figure 2.6: HI bound-free extinction coefficient $\sigma_\nu^{\rm bf}$ per hydrogen atom in level n (here written as α_n) against wavelength. The Lyman, Balmer, Paschen, Brackett and Pfund edges are marked by the quantum number n of the ionizing level. Their amplitudes increase with n and have not been added up in this figure. The threshold wavelengths are specified in Table 6.1 on page 156. Even in the peaks, the bound-free extinction per particle is much smaller than the profile-integrated extinction of a resonance line given by (2.58). From Gray (1992).

from Rutten

Free-free transitions. Free-free transitions have $S_\nu = B_\nu$ when the Maxwell velocity distribution holds ("thermal Bremsstrahlung"). The corresponding volume extinction

Fig. 2.—

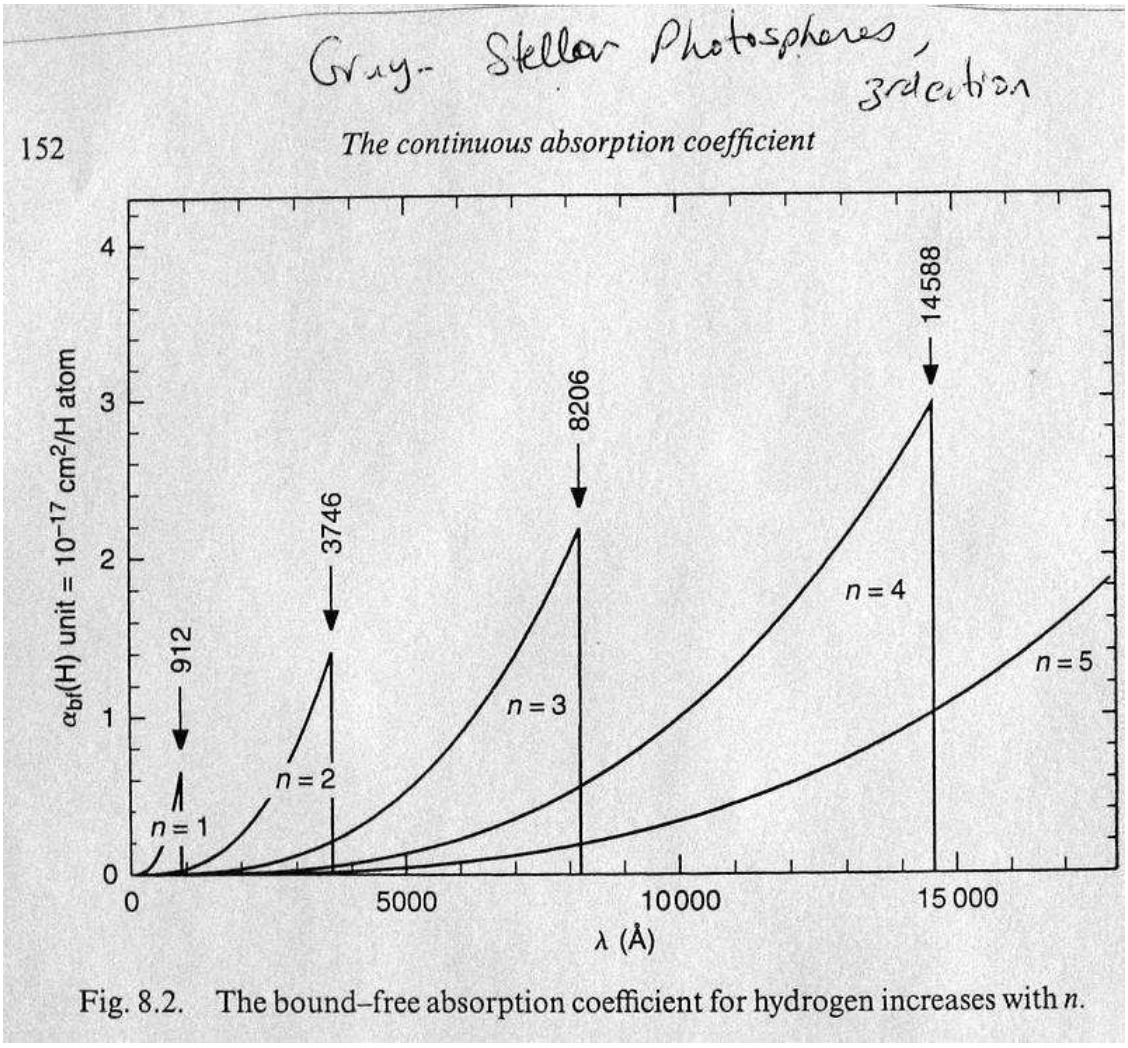

Fig. 8.2. The bound–free absorption coefficient for hydrogen increases with n.

Fig. 1.— The bound-free absorption coefficient for H. (Fig. 8.2 of Gray)

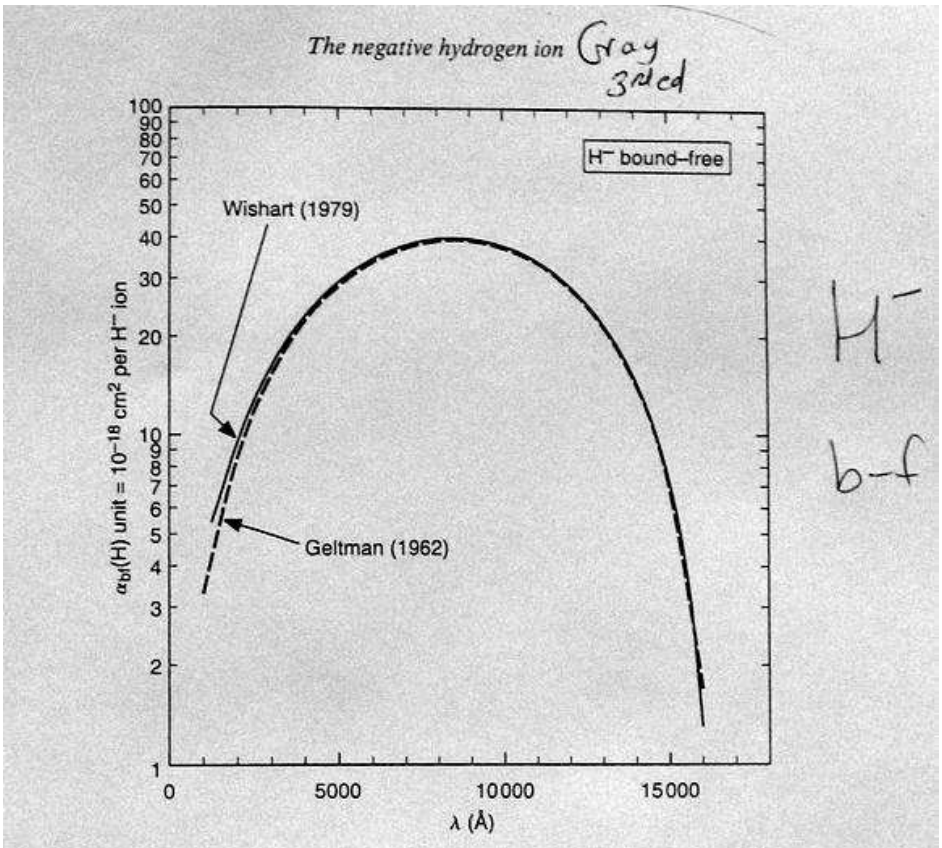

Fig. 8.3. The absorption coefficient of the negative hydrogen ion shows a maximum near 8500 Å. Two calculations are compared.

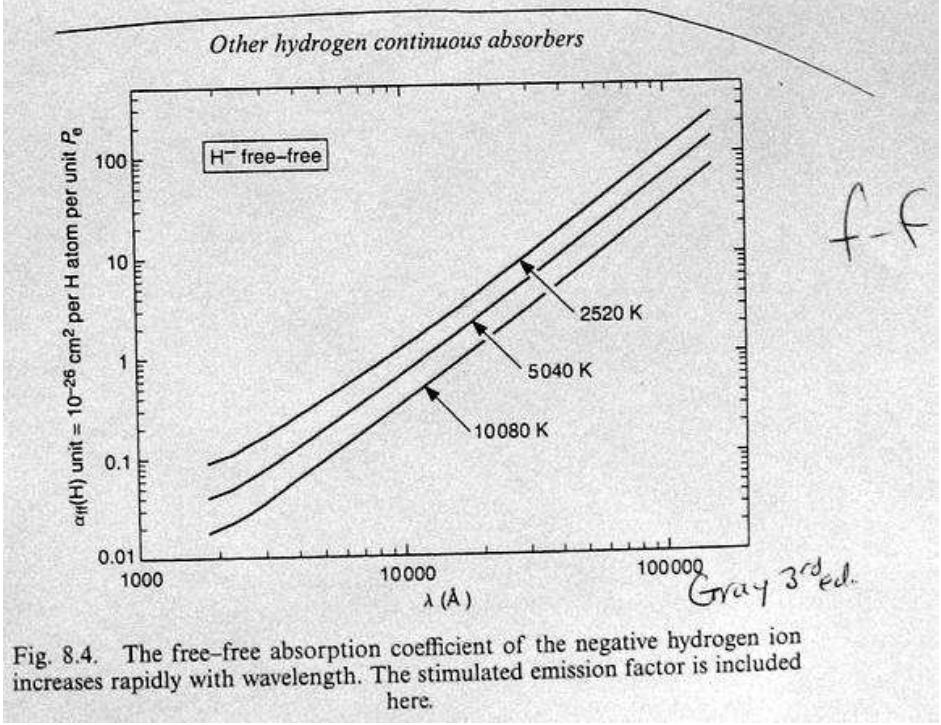

Fig. 8.4. The free–free absorption coefficient of the negative hydrogen ion increases rapidly with wavelength. The stimulated emission factor is included here.

Fig. 2.— The bound-free and free-free absorption coefficient for H^-. (Fig. 8.4 of Gray)

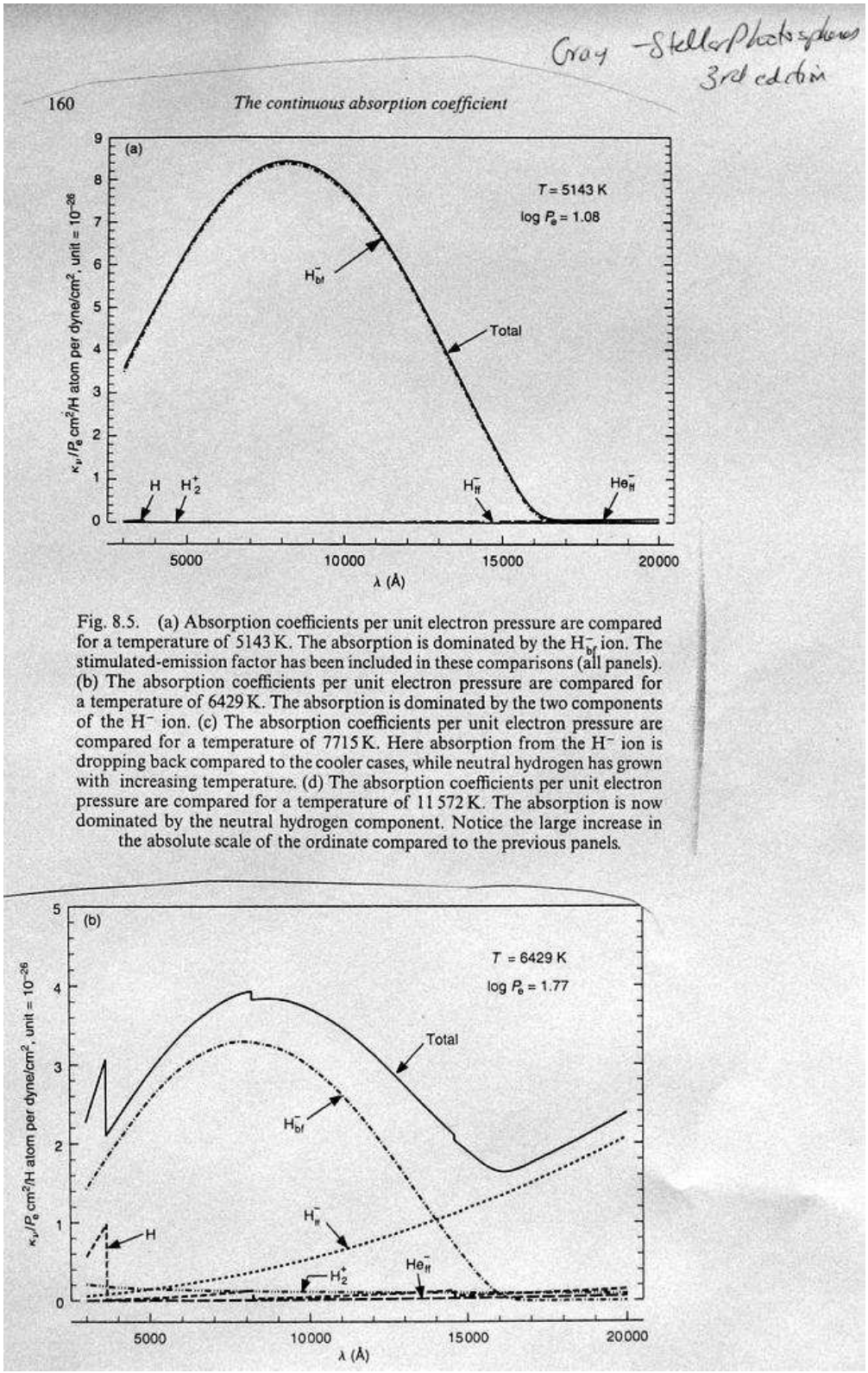

Fig. 3.— The contributions to the total opacity for low temperatures. (Fig. 8.5 of Gray)

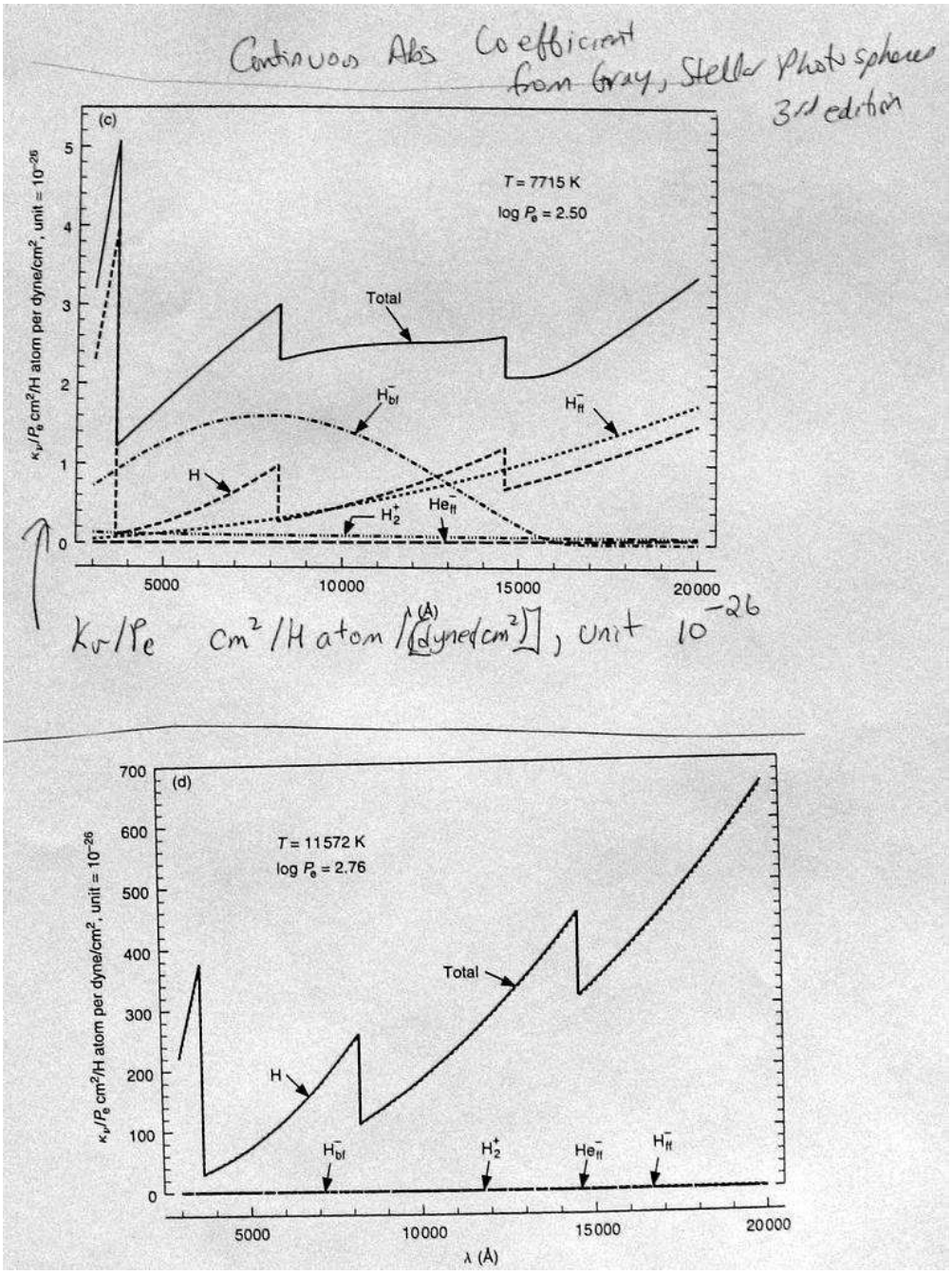

Fig. 4.— The contributions to the total opacity for higher temperatures where the contribution from H dominates. (Fig. 8.5 of Gray, additional panels)

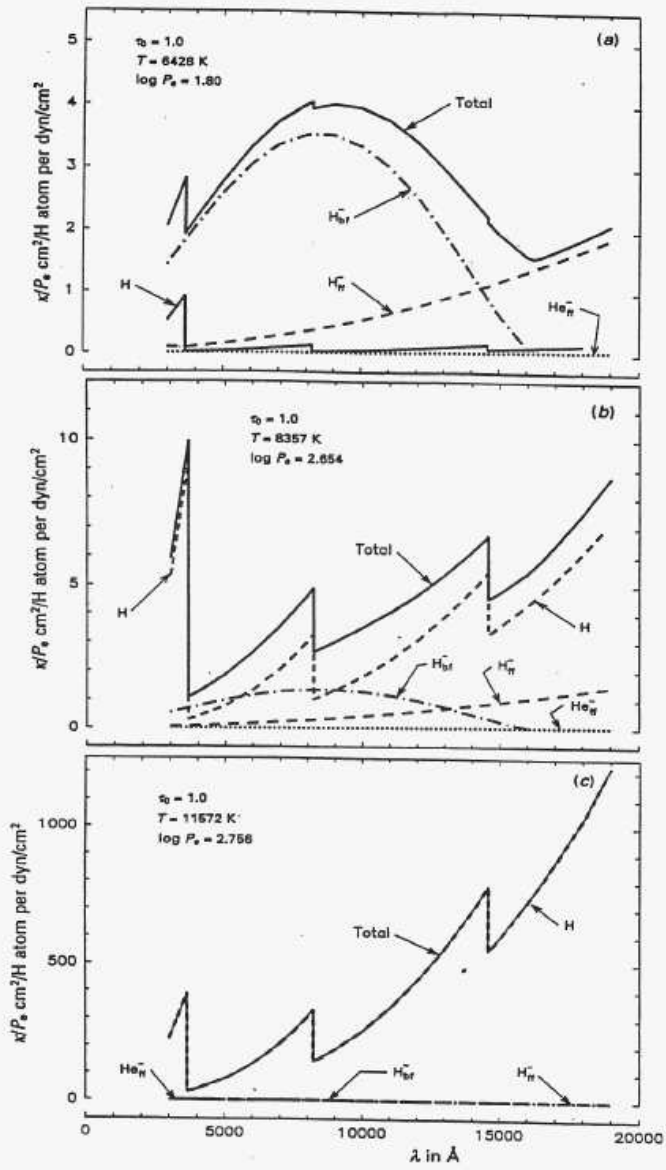

from Rutten

Figure 6.14: Continuous extinction coefficients κ_ν^c from hydrogen and helium, per neutral hydrogen atom and per unit electron pressure, for the depth $\tau_0 = 1$ (continuum optical depth at $\lambda = 5000$ Å) in the photospheres of three dwarf stars. The coefficients κ are here measured per neutral hydrogen atom in whatever state of excitation, assuming Boltzmann population ratios, and normalized by the electron pressure because the H^-/H density ratio scales with P_e. Panel (a) is for the Sun, panel (b) for a late A dwarf, panel (c) for a late B dwarf. The curves do not extend beyond the Balmer edge at left where the metal edges become important. From Gray (1992).

Fig. 4.—

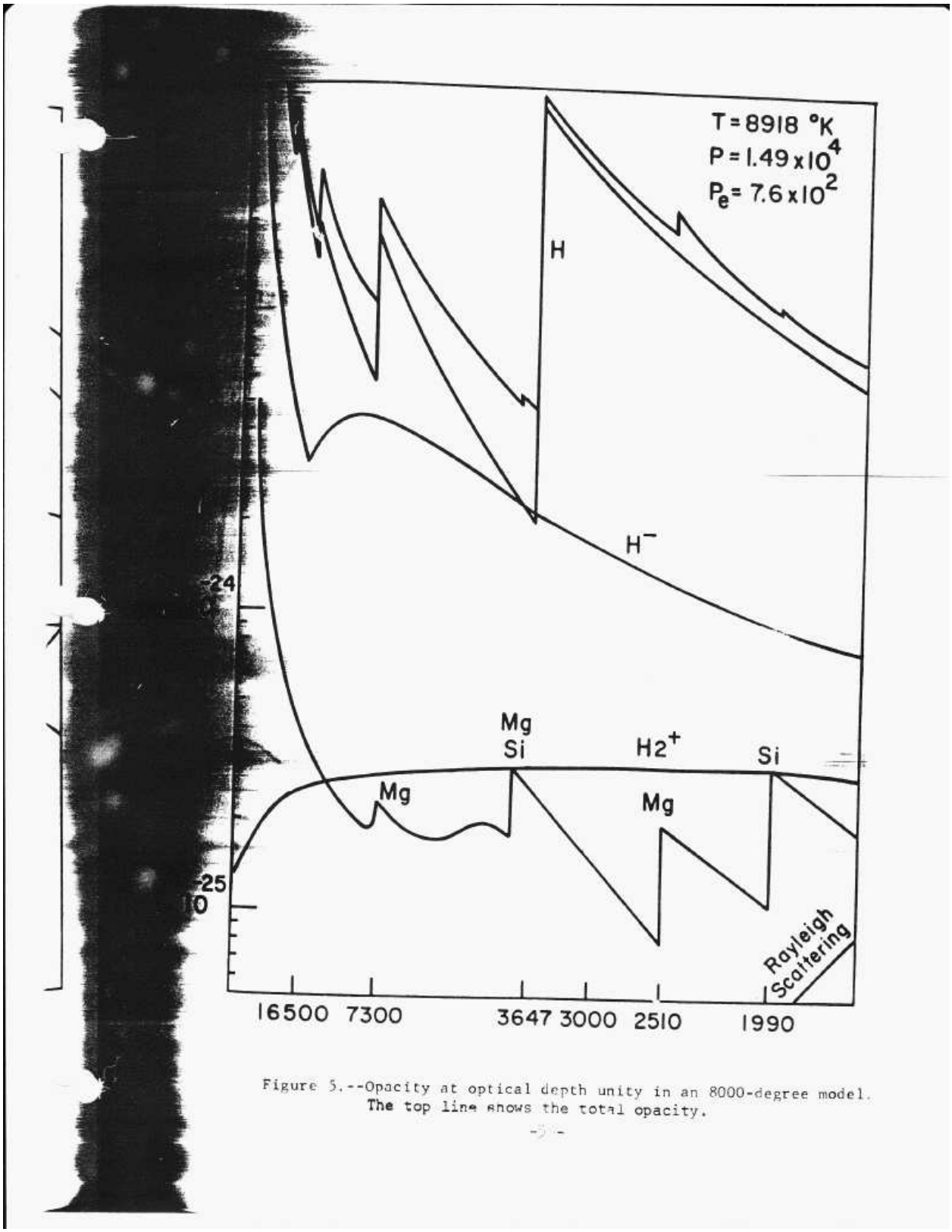

Figure 5.--Opacity at optical depth unity in an 8000-degree model. The top line shows the total opacity.

Fig. 5.— from Kurucz

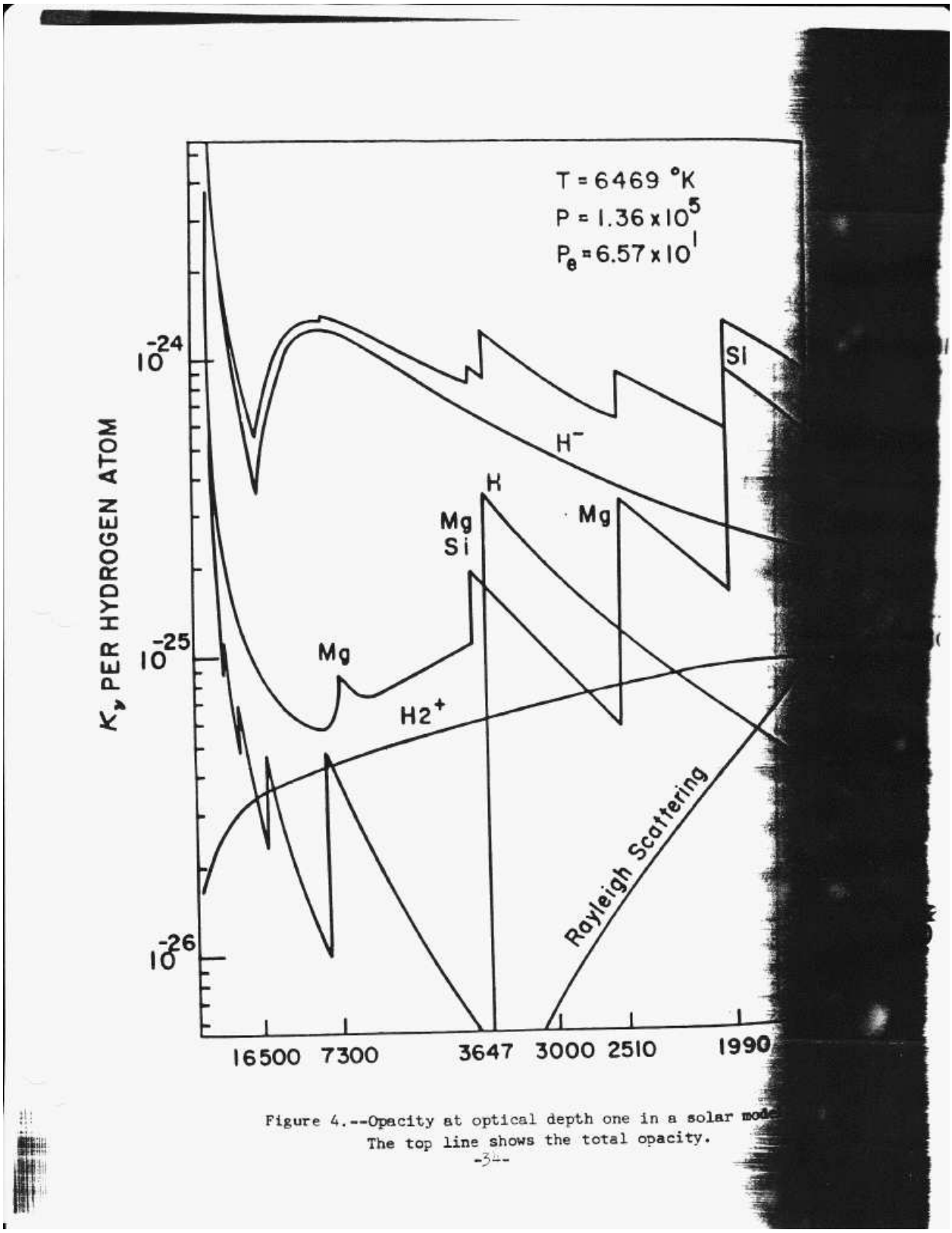

Figure 4.--Opacity at optical depth one in a solar mode
The top line shows the total opacity.
-34-

Fig. 6.— from Kurucz

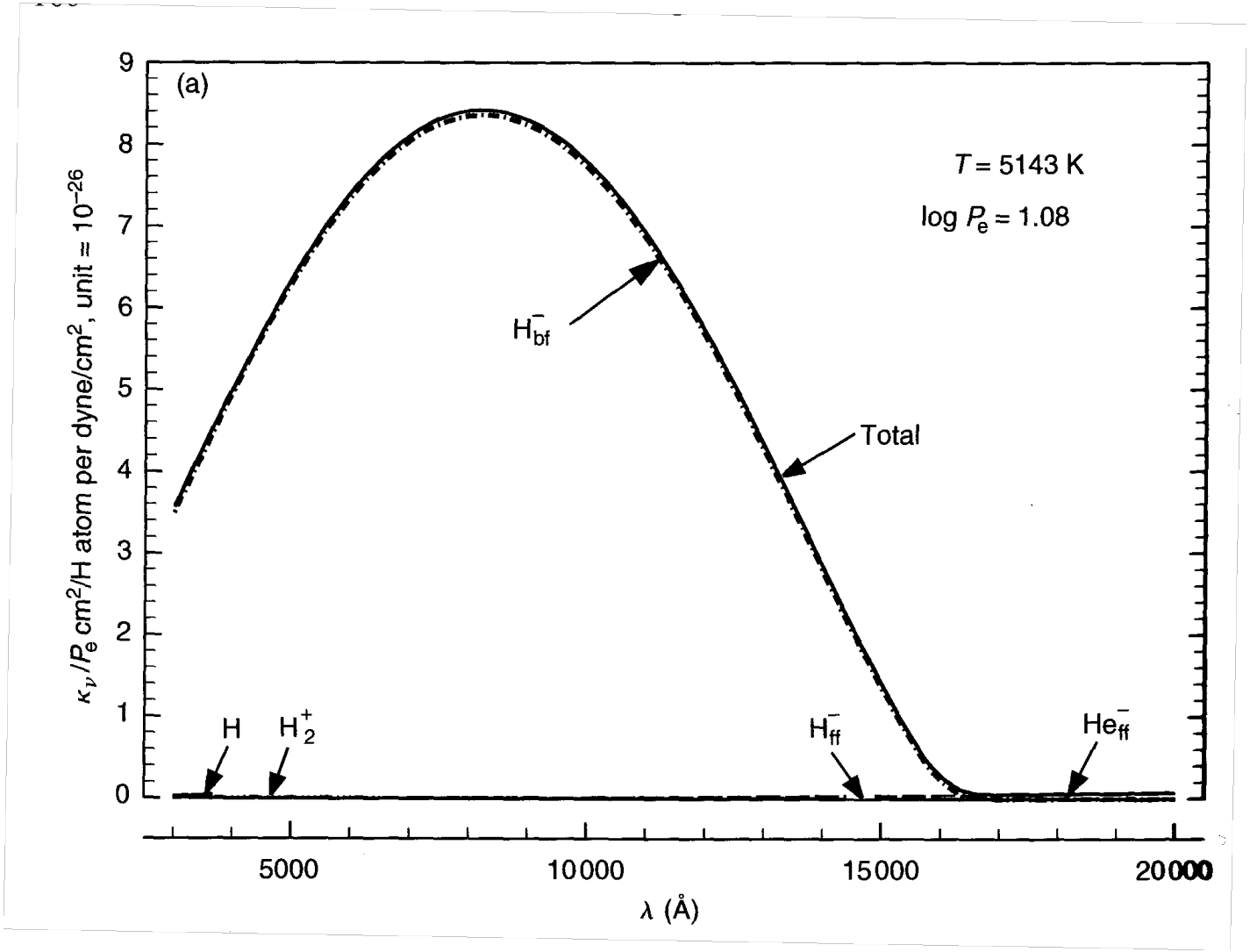
(a)
T = 5143 K
log P_e = 1.08
H^-_{bf}
Total
H
H^+_2
H^-_{ff}
He^-_{ff}
κ_ν / P_e cm^2/H atom per dyne/cm^2, unit = 10^{-26}
λ (Å)
0
1
2
3
4
5
6
7
8
9
5000
10000
15000
20000

Gray, Fig. 8.5a

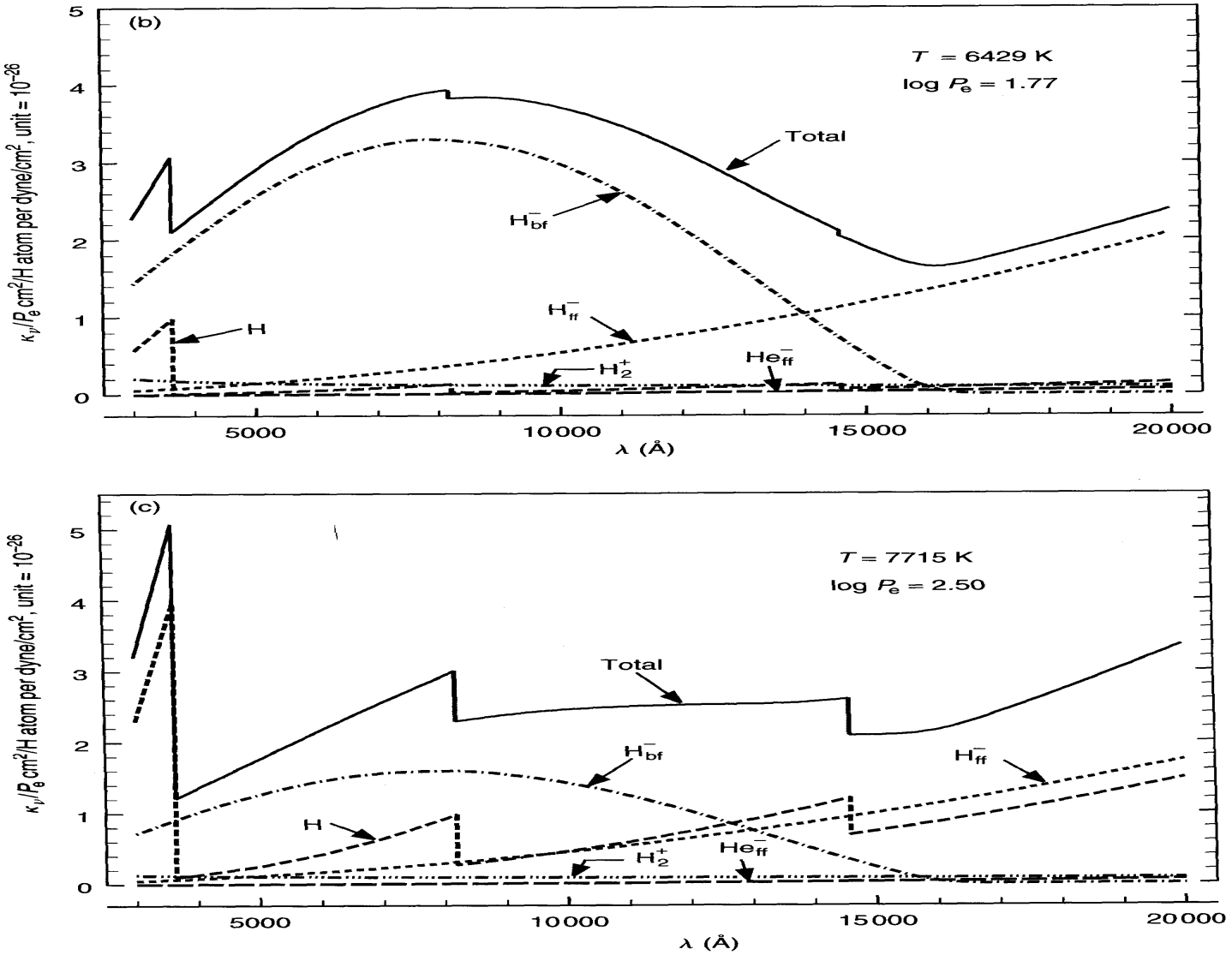

Fig. 8.5. (*cont.*)

8.5c

Figure 7.4. Schematic plot of $\log\kappa$ versus $\log T$ for fixed ρ. Recall that power laws appear as straight lines in a log-log plot.

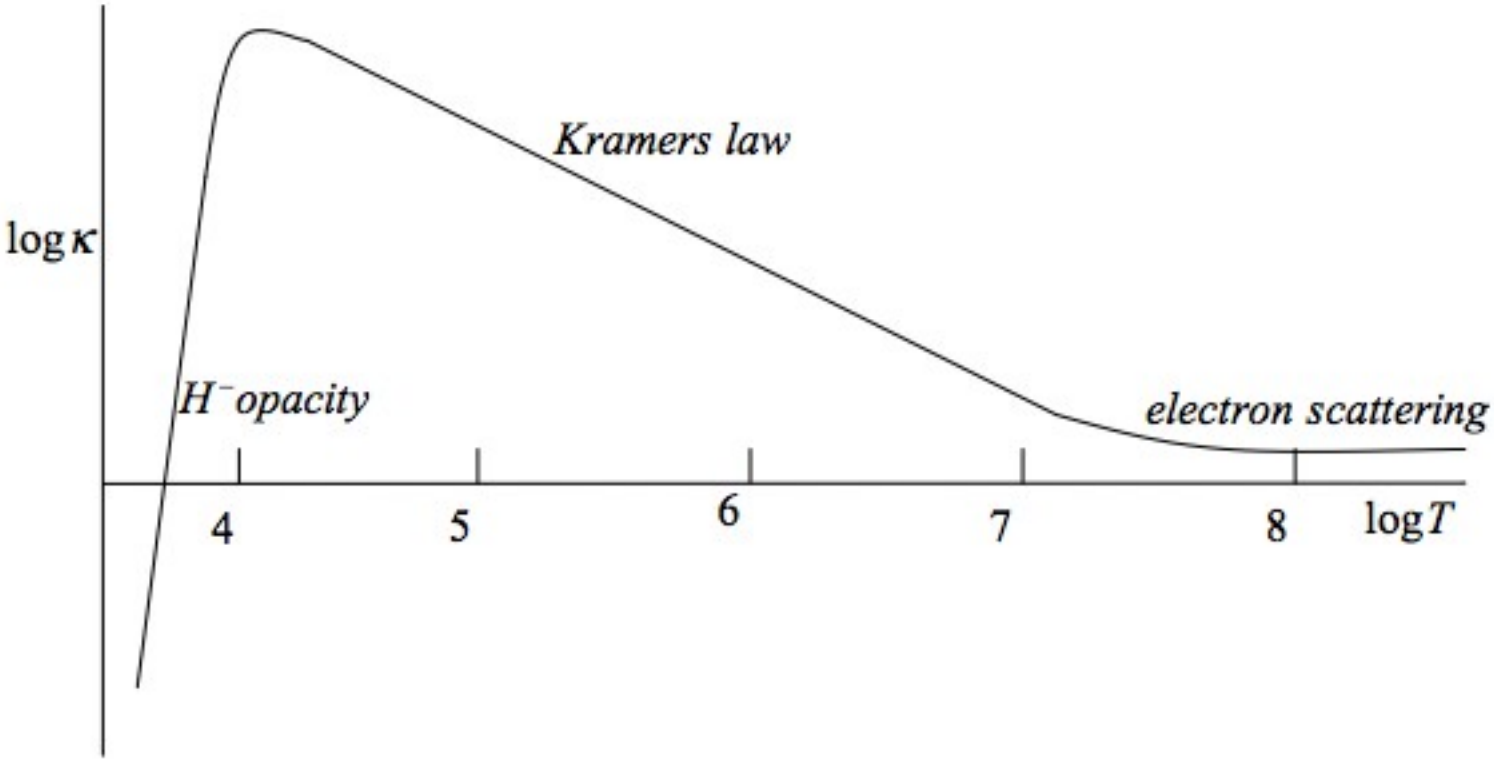

From Stan
Woosley
10/17/15

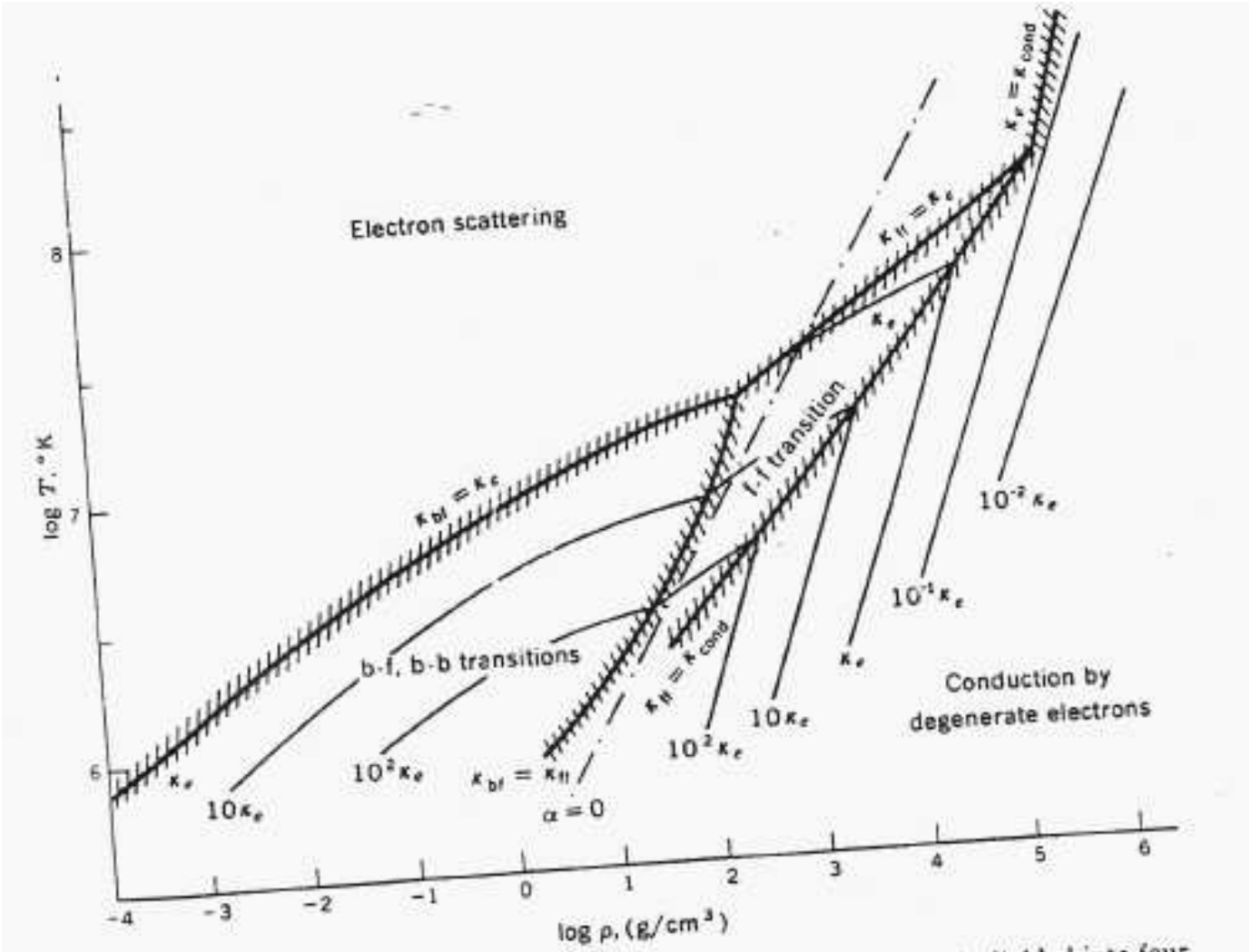

Fig. 3-15 The total opacity of population I composition. The ρT plane is divided into four domains according to which opacity source is the most important for energy transport, electron scattering, bound-free transitions, free-free transitions, and conduction by degenerate electrons (to be discussed in Sec. 3-4). The lines designating these boundaries are cross-hatched. Contours of constant opacity are labeled by the value of κ in terms of the opacity κ_e due to electrons. A dashed line shows where the degeneracy parameter $\alpha = 0$. (After C. Hayashi, R. Hoshi, and D. Sugimoto, *Progr. Theoret. Phys. Kyoto, Suppl.* 22, 1962.)

Fig. 7.— from Clayton, "Principles of Stellar Evolution and Nucleosynthesis"

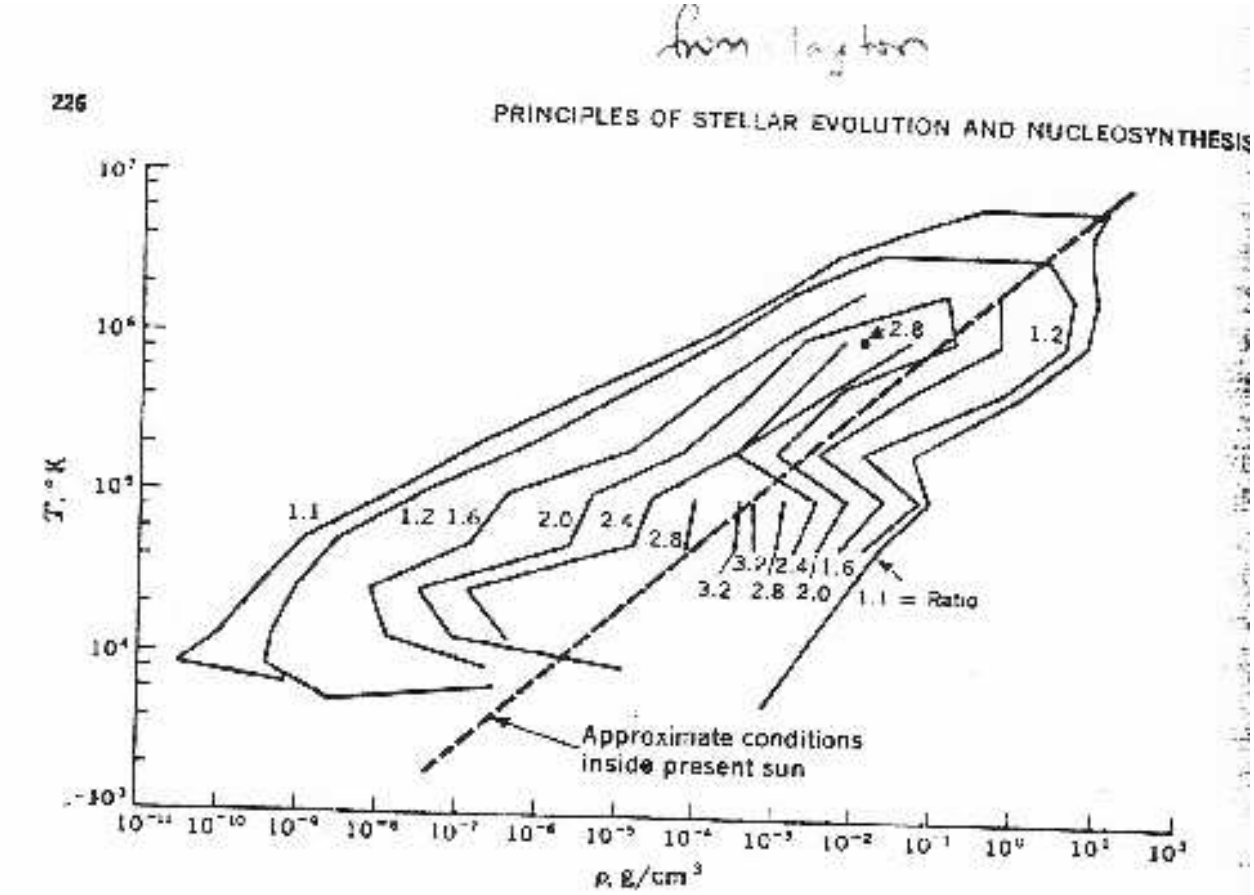

Fig. 3-17 The ratio of the total radiative opacity with discrete atomic lines included to its value without the discrete lines. The conditions within the sun are shown as a point of reference. It can be seen that atomic transitions increase the value of the opacity by a significant factor in the sun. *[Reprinted from A. Cox, Stellar Coefficients and Opacities, in L. H. Aller and D. B. McLaughlin (eds.), "Stellar Structure," The University of Chicago Press, Chicago, 1965. By permission of The University of Chicago Press. Copyright 1965 by The University of Chicago.]*

Fig. 8.— This is a $\rho - T$ plane, with T ranging from 10^3 to 10^7 K and $\rho = 10^{-11}$ to 10^2 gm/cm^3.

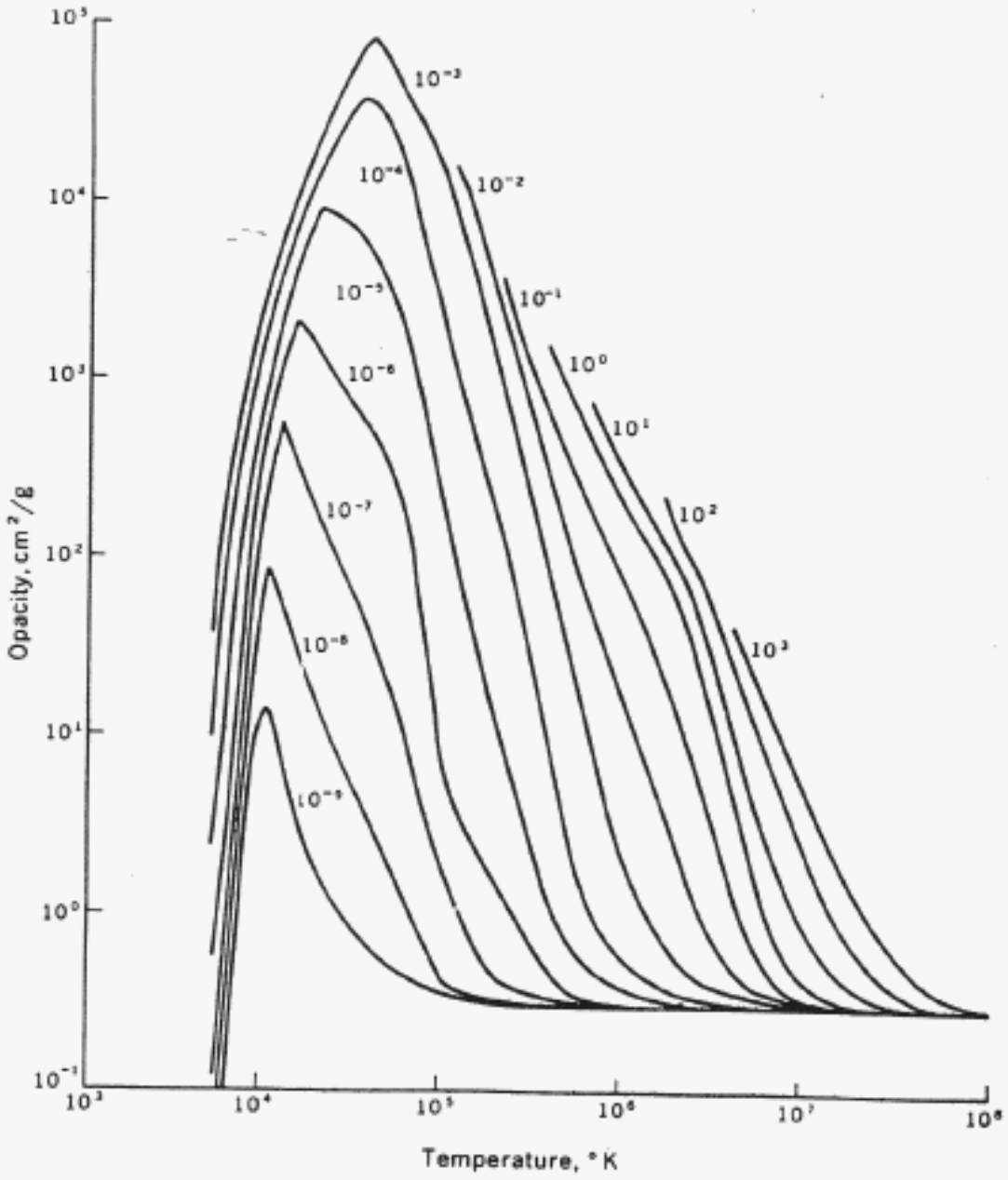

Fig. 3-16 The total opacity of material of solar composition as a function of temperature. Each curve is labeled by the value of the density. The range of values shown was chosen to illustrate the characteristic values of the opacity within the sun. [*After D. Ezer and A. G. W. Cameron, Icarus*, **1**:422 (1963).]

Fig. 9.—

OPAL Project

 ApJ 371, 408, 1991

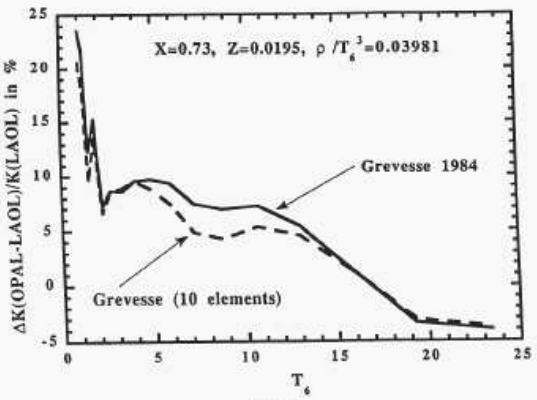

FIG. 2a

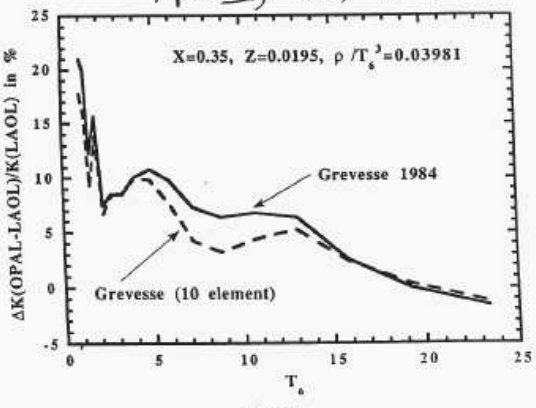

FIG. 2b

FIG. 2.—Comparison of OPAL and LAOL opacity results for the Grevesse (1984) mixture along density-temperature tracks defined by ρ/T_6^3 as indicated in the figures. Here, LAOL results in BU are used as standard.

abundances). With each additional element, a small amount of hydrogen is replaced with a more efficient absorber, thus producing an increase in opacity. For the preferred scheme, with each additional new element, both a lighter and heavier element are reduced in abundance and the direction of change depends on the detailed absorption properties of the elements in question. As a result, the opacity can decrease slightly when an element is added to the mixture.

Our calculations for the Rosseland mean opacities are presented in Tables 2–5 for the 15 element mixtures mentioned above. The definitions follow those used in BU: T_6 denotes the temperature in units of 10^6 K, X denotes the hydrogen mass fraction, Z denotes the metallic mass fraction, and the density-temperature follows a track of constant ρ/T_6^3 with ρ in g cm^{-3}. There are three density-temperature tracks for each pair of X and Z in Tables 2–5, and there are four such pairs.

The results for the Grevesse composition are compared in Figure 2 with the LAOL results in BU taken as the standard for reference purposes. Our results are a few percent higher near the solar center ($T_6 \sim 16$, $X = 0.35$) and about 10% higher near the bottom of the convection zone ($T_6 \sim 2$, $X = 0.73$). Note in Figure 2 that our 10 element version of the Grevesse mixture in Table 1 can be as much as 3% below the 15 element calculation.

Results for the other mixtures are presented in Figure 3 where now the OPAL result for the Grevesse mixture is used as the standard. The opacity variations seen when comparing these solar mixtures can be as large as 10% and, therefore, comparable to variations between the LAOL and OPAL codes. By including the additional compositions, it should be possible to study the sensitivity of solar models to element abundances using OPAL opacities as previously done for the

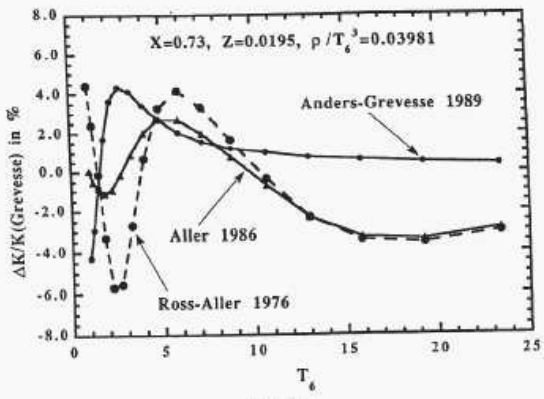

FIG. 3a

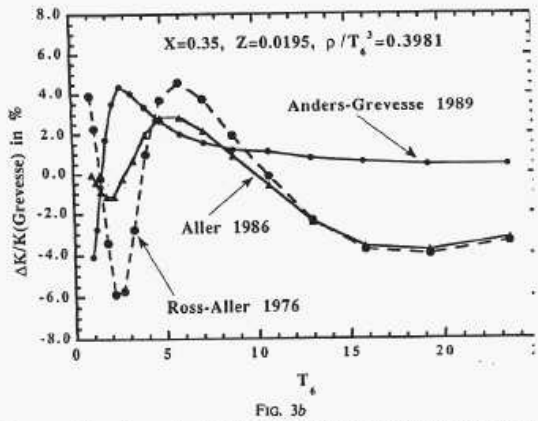

FIG. 3b

FIG. 3.—Comparison of OPAL Rosseland mean opacities for different chemical composition along a density-temperature track with the OPAL result for t Grevesse (1984) mixture as standard.

Fig. 10.—

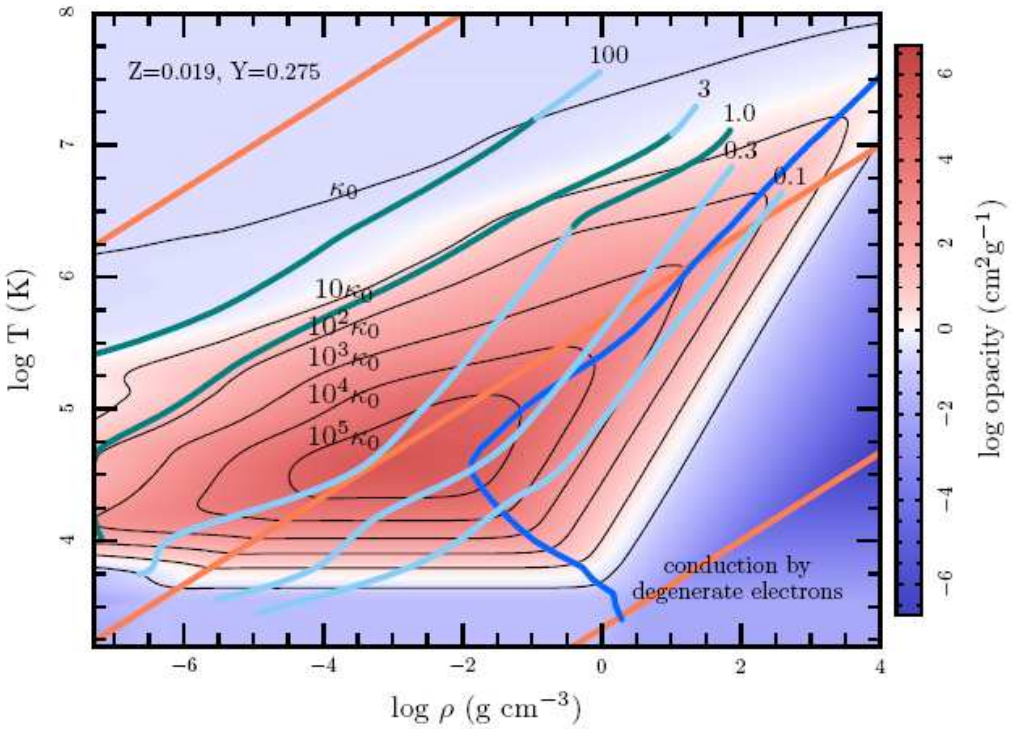

Fig. 3.— The resulting MESA opacities for $Z = 0.019, Y = 0.275$. The underlying shades show the value of κ, whereas the contours are in units of the electron scattering opacity, $\kappa_0 = 0.2(1 + X)$ cm^2 g^{-1}. The orange lines show (top to bottom) where $\log R = -8$, $\log R = 1$ and $\log R = 8$. Stellar interior profiles for main sequence stars of mass $M = 0.1, 0.3, 1.0, 3.0$ & $100 M_\odot$ are shown by the green(radiative regions)-light blue(convective regions) lines. Electron conduction dominates the opacity to the right of the dark blue line (which is where the radiative opacity equals the conductive opacity).

Fig. 11.— Total opacity from the MESA code for a specified value of H and He as a function of temperature and density.